4

Abundance of O, Na and Al in stars of GC M3, M4, M13 and M6752

4.1 Introduction

Globular cluster (GC) stars are known to display homogeneous abundance patterns for Fe-peak elements but significant abundance variations are seen among the light elements. Na-O and Mg-Al anticorrelations are also observed among the stars of GCs (Kraft (1997)[72], Gratton et al. (2004)[31], Carretta et al. (2009a)[220], Smolinski et al. (2011)[221]) etc

and references therein). The inhomogeneities and abundance variations observed in light-elements increases with decreasing metallicity. For instance, C, N, O and Na abundances in giants of M7 with an average metallicity ([Fe/H]) of ~ -0.7 show mild variations compared to their counterparts observed in giants of M5 with a metallicity of ~ -1.2. Several studies both observational and theoretical in literature are devoted to the understanding of the complex abundance patterns of GCs (Cordero et al. (2015)[222], Roederer et al. (2015)[223], Spite et al. (2016)[224], Villanova et al. (2016)[37]). The origin of the observed abundance anomalies, however,still remain poorly understood. GCs span a wide range in metallicities with $[Fe/H]$ as small as -2.38 upto as large as $+0.12$ (Table 2 Gratton et al. (2004)[31] and references therein). Here amongst the chosen GCs, GC M3 has an average metallicity of -1.39 and is more distant to M5. The scatter among the light elements and the enhanced odd atomic numbered elements typically seen in metal-poor GCs are also noticed in M3, although at a lower level of star-to-star variation (Cohen et al. (2005)[225]). GC M13 with an average metallicity -1.50 is known to show a large star-to-star differences in the abundance of Al, Mg, Na, and O among its red giants Cohen et al. (2005)[225] references therein. GC M4 is the closest to us (Dixon et al. (1993)[226]) and has an average cluster metallicity of -1.17 (Liu et al. (1990)[227], Drake et al. (1992)[228], Drake et al. (1994)[229]). A characteristic feature observed in the colour-magnitude diagrams of GC M4 stars is the presence of broadened red-giant branches (Marino et al. (2008)[230]). The two giant branches appear to correlate with typical globular cluster variations in [O/Fe] and [Na/Fe] abundances rather than variations in total [C+N+O/Fe] abundance (Martell et al. (2011)[231]). Detailed elemental abundances are available for a large number of stars belonging to this cluster. The largest spread in light element abundances is known to be observed in GC NGC 6752. This GC has been studied by many groups including (Yong et al. (2005)[33]), and the reported average cluster metallicity due to (Yong et al. (2005)[33]) is ~ -1.61 . But the common feature of these four GCs is the observed Na-O and Mg-Al anti-correlation. The proton-capture chains that convert C

and O to N, Ne to Na and Mg into Al in the hydrogen-burning layers of evolved stars are believed to be responsible for these observed trends; however, the astrophysical site(s) for their occurrence is still under debate. Amongst the contesting scenarios one is *evolutionary* which considers deep mixing of the stellar envelope through the hydrogen burning shell that brings the products of proton-capture chains to the surface. And the other one is *primordial* where observed abundances originated from proton-capture synthesis that took place in some earlier generation massive stars whose interior can easily attain a high temperature so that advanced H-burning can be sustained. However recent spectroscopic studies have challenged the former one as it possibly can't explain why a similar kind of abundance anomalies is present even in stars which are below and above the main sequence turn-off (Decressin et al. (2007b)[130]). Also the evolutionary scenario can't explain why the stars of GC ω Cen which is the most massive cluster, have found with a large spread in metallicity and thereby throwing out the earlier paradigm that the GCs are examples of "Simple Stellar Populations"(SSP) (D′Ercole et al. (2008)[232]). Under the currently favoured astrophysical sites where the processing of element takes place, as well as the mechanism by which processed material is subsequently delivered into new generations of stars are (i)the massive AGB stars [232], (ii) the fast-rotating massive main sequence stars (Decressin et al. (2007b)[130]) and (iii) the massive interacting binaries [233]. In "AGB star" during Hot Bottom Burning (HBB), the CNO elements undergo p-capture nucleosynthesis which is found to be sensitive to metallicity of the star (Ventura et al. (2013)[234]). But this HBB, for any effective depletion of oxygen abundance due to p-capture reaction, requires a high temperature as high as $T_9 > 0.1$ (Ventura et al. (2013)[234]). Again at high temperature the destruction channel for sodium is dominant compared to the production reaction by p-capture on ^{22}Ne nuclei, thus the sodium previously accumulated at the surface is destroyed (Denissenkov & Herwig (2003)[235], Ventura et al. (2013)[234]. This points towards correlation between Na and O abundance which in fact has been confirmed by a recent study performed by (Ventura et al. (2013)[234]) at very

low metallicity unless the polluted material which is lost from the surface of the stars via slow winds suffer a certain amount of dilution with pristine (Ventura et al. (2013)[234]) to have Na-O anticorrelation, which is then remain trapped within the gravitational potential of the cluster. As mentioned earlier, these four GCs have shown Na-O anticorrelation, three of which has been already reported in a recent study performed by (D′Antona & Ventura (2007)[236]) considering some new stellar models. Again in the third scenario i.e. interacting massive binary stars may provide an efficient way to lose large amounts of processed material that could be incorporated into an enriched population. This scenario is attractive because a large fraction of massive stars are indeed observed to be members of binaries that will interact during their lifetime (Sana et al. (2013)[237]). Again de Mink et al. (2009)[233] has assumed a non-conservative evolution of massive close binaries which may not be correct because the mass that is lost by the loser (the primary one) leaves the binary as a slow wind driven by the rotation of the gainer (the secondary one) and takes with the specific orbital angular momentum of the gainer. Thus this will lead to the merger of the binary and the evolution will be different as suggested by the same author (Vanbeveren et al. (2012)[238]. In the “winds from fast rotating massive stars" (WFRMS) scenario (discussed in section 5.3), it is assumed that massive stars within GCs rotate near break-up speed. Processed material is brought to the surface by rotational mixing, lost via a mechanical wind, and then accumulates in a disk around the star, where the second generation of (low-mass) stars is assumed to form (Decressin et al. (2010)[239]).

4.2 Why Massive stars?

The collapse of a giant molecular cloud (GMC) ($\sim$ 100-1000 $M_{\odot}$, Zinnecker & Yorke (2007)[249]) having typical number density of $H_2 \sim 10^5$ cm^{-3} (Jappsen et al. (2005)[250]) and temperatures of 10-20 K is mainly governed by the gravitational pressure, which leads to accumulation and eventual fragmentation. The Jeans mass provides an approximate criteria

for the occurence of such a collapse and once the gas exceeds the Jeans mass, it will begin to contract on a free-fall timescale where $\tau_{ff} \propto \rho^{-1/2}$ (Shu, Adams & Lizano (1987)[251]). The released gravitational binding energy is trapped in the protostar which is then followed by an accretion disc which results in sealing of most of the in-falling matter while their central temperature increases towards that required temperature ($T_c \geq 3 \times 10^7$ K) to initiate the fusion of hydrogen into helium. However during evolution some part of the mass goes off because of bipolar outflows. Though in the MS stage the size of the envelope expands but strong mass loss may shrink the envelope. However how much mass a massive star loses during its life depends strongly on its initial mass, rotation rate and metallicity (Meynet & Maeder (2005)[252]). High metallicity and rotation rate boost mass loss. Massive stars have MS-lifetimes of a few to a few tens of millions of years. During the early stages of H burning, massive stars finally destroy their “parent" cloud by strong radiation and winds. Thus as pointed out by Haiman & Loeb (1997)[240] the massive star are involved in re-ionizing the universe which played a crucial role in subsequent evolution. Moreover because of their high luminosities (10^4-10^6 $L_\odot$) they are visible from distances even at high redshifts (e.g.,Douglas et al. (2009)[241]) whose radiation pressure may involve in star-formation. Not to mention about their deaths by supernovae (Mezzacappa (2005)[254]) can bring new horizon not only to the study of their evolution at different metallicities (Savaglio (2006)[242]; Ohkubo et al. (2009)[243]) but also can be used for probing intervening structures of the universe. Other energetic phenomenon, such as Gamma Ray Bursts (GRBs), were also recently linked to massive stars (Woosley & Bloom (2006)[244]), strong radiation winds (Getman et al. (2009)[245]) and SN shocks (Preibisch & Zinnecker (2007)[246]) not only can trigger star formation activity but also affect planet formation (Bally et al. (2005)[247]) as well as structure of galaxies (Kennicutt (2005)[248]) too. The end of the MS is marked by the exhaustion of H in the stellar centre. However H can still burn in the shell around the core, which may lead to an expansion of the envelope, while the core still contracts until He

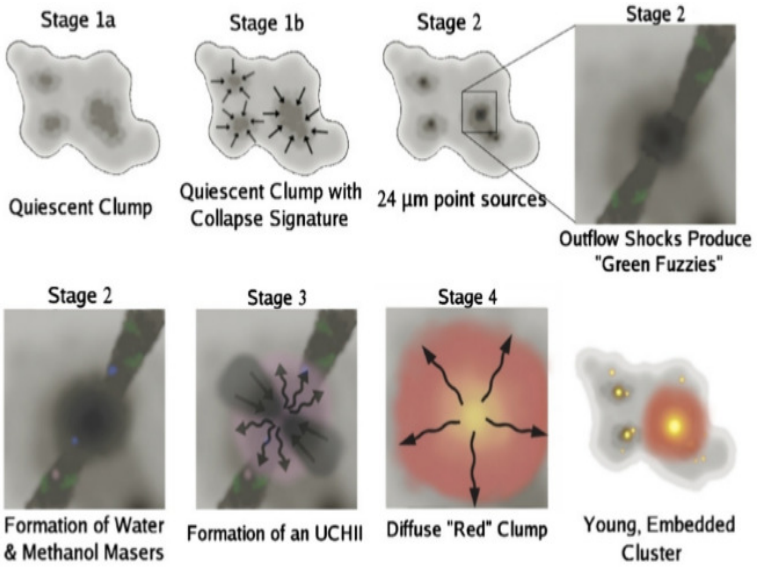

Fig. 4.1 A diagram showing the formation of massive star: 1.) accumulation, 2.) collapse, 3.) accretion, 4.) disruption of the birth cloud (Battersby et al. (2010)[253]).

burning starts. The fusion of He to C begins once $T_c \approx 1.5 \times 10^8$ K is reached. The central He-burning phase lasts about 10% of the MS-lifetime. Thus a star spends most of its lifetime either in the H- or He-burning phase. The ashes of He burning consist of C and O. During C-burning phase, C fuses to form Ne and Mg, next Ne-burning will lead to the formation of O and Mg and then O and Mg to Si and S during an O-burning phase and finally in Si burning, Si and S are built into iron group elements like Ni, Fe and Cr for stars with M$\gtrsim$10 $M_\odot$. Each burning modes will take place at different temperature with increase in value from $T_c \gtrsim 6 \times 10^8$ K for C burning to $T_c \gtrsim 3.5 \times 10^9$ K for Si burning with lesser and lesser timescale as the temperature increases. Because the maximum of nuclear binding energy is around Fe, stars cannot gain energy by fusion after Si burning. This gives a massive star an onion shell (Fig. 4.2) like structure at the time of iron core collapse. For stars more massive than about 10 $M_\odot$, after central Si exhaustion they starts to contract and the core reaches nuclear statistical equilibrium in hydrostatic conditions. Thus nucleosynthesis is therefore a "by-product" of stellar energy generation, and the burning phases explain the origin of the majority of the elements between carbon and iron.

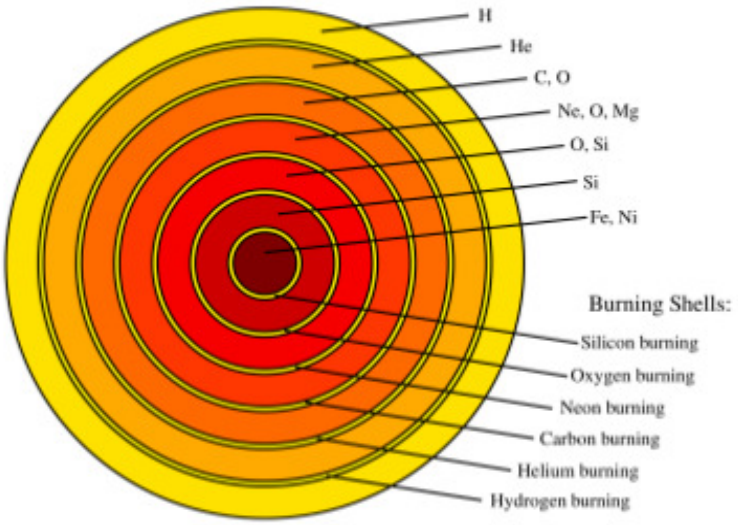

Fig. 4.2 Schematic stellar structure of massive stars before their death. On the upper right the most abundant elements of the different layers are shown, while at the lower right the burning shells are indicated. Figure courtesy of C. Winteler.

4.3 WFRMS scenario: The Basic Physical Situation

Classical models of stellar evolution focus on the dominant role of various stages of nuclear burning in the stellar core. Not only the temperature is crucial in any stellar situations but density also plays an important role. Even though the density ranges from many orders of magnitude its response in the burning rates is only linear and hence its importance is much less significant as far as the elemental synthesis is concerned unless one considers a situation where low temperature and high density is prevailing. The materials are synthesized in the inner regions near to the core and are brought to the surface by means of some physical mechanisms like convection or by dredging up mechanisms. Here the stars are assumed to be spherically symmetrical with no magnetic field, no rotation and no mass loss from the surface. And the process of convection is only the mixing mechanism with the convective regions and are always fully mixed (Salaris et al. (2002)[287]) which is the canonical model of star. But in recent years it has become clear that stellar evolution, particularly for more massive stars, can also be profoundly influenced by the loss of mass and angular momentum from the stellar envelope and surface (Maeder& Meynet (2008)[269]). Models of the MS evolution

of rotating massive stars show that, at the surface, the velocity approaches a critical limit. This is induced by internal evolution of stars that results in transport of angular momentum from the contracting, faster rotating inner convective core to the expanding, slowed down radiative envelope (Meynet et al. (2006)[270]). However beyond the critical limit any further increase in rotation rate is not dynamically allowed, hence the further contraction of the interior is then balanced by a net loss of angular momentum through an induced mass loss. Here this mass loss is assumed to be isotropic. Thus the sythesized mass by the star will now be delivered to the ISM. And hence the ISM is pre-enriched with material those have produced by other stars. Moreover the materials are assumed to be released in the ISM with a very low velocity and thus can easily be retained into the potential well of the globular cluster. Here we assume the density of the stellar matter constant which in general, is not a sensitive parameter unless one goes to a high value $\sim 10^5$ gm/cc or even higher where pycnonuclear type of reaction has to be considered. We also assume the star to be in equilibrium and thereby making it to maintain a balance between the produced energy due to thermonuclear fusion and the loss of energy at the surface. Thus the temperature of the star can essentially assume to be a fixed quantity. Here we mainly focus on which type of stars did produce the material enriched in H-burning products and how? However we do not comment on the physical factors that influence the mass loss neither we look for what is the physical mechanism responsible for selecting only material bearing the signatures of H-processing those have been lost? The following paragraphs describes briefly the nucleosynthesis related to hydrogen burning relavent to our study that massive stars experience.

CNOF cycle:

Here the steps involved the nuclear burning cycle have been outlined. A brief discussion of few of the (p,γ) reactions involved have been discussed in the next chapter. At low temperature, density condition the ^{12}C(p,γ)^{13}N reaction can compete with p-p reaction and thus can initiate the CNO burning mechanism (Clayton 1983[255] and ref. in here). ^{13}N is β

unstable and decays to ^{13}C in a time scale of 862.77 sec (Audi et al. (2003)[256]) since its proton capture lifetime is quite large in the considered temperature density condition. On the other hand ^{13}C is a stable isotope of carbon with relative abundance 1.1078 (Lodders (2003)[257]). This ^{13}C forms ^{14}N by taking a proton and then ^{14}N to ^{15}O taking a proton again. ^{15}O then decays via a β emission to ^{15}N in an average lifetime of 176.39 sec (Audi et al. (2003)[256]). Here ^{15}N branching appears. The table 4.1 shows the branching ratios of the cycle at various temperatures. The rate constants for ^{15}N are taken from NACRE compilation and for ^{17}O are taken from Iliadis et al. (2010)[133]. These branching ratios show that the (p,α) reaction wins over the (p,γ) reaction and thus confirming the cyclic behaviour forming ^{12}C by most of ^{15}N nuclei. This is the CN cycling. The branching ratio will guide how much of ^{15}N will go to form ^{16}O by taking a proton. This point onwards the oxygen-fluorine reaction network starts,of which discussion is available in many places in the literature (Bekki (2011)[258], Cameron et al. (2013)[259]). Here we give a brief description relevant to this work. A proton capture by O^{16} leads to the formation of unstable F^{17} which decays into ^{17}O. This secondary isotope of oxygen has very small relative abundance (Lodders (2003)[257]). This is probably due to the fact that O^{17} gets destroyed via both $O^{17}(p,\alpha)N^{14}$ and $O^{17}(p,\gamma)F^{18}$; the former reaction rate is higher compared to the later one at the same temperature condition. Thus the (p,α) reaction also has its importance for further evolution and starts competing with (p,γ) reactions. The inclusion of the (p,α) reaction which has also been considered here, introduces another branching point in the cycle, of which the branching point ratio of (p,γ) to (p,α) which has been shown in (Table 4.1). If the cycle advances forming ^{18}F then this will be immediately followed by $F^{18}(e^+,\nu_e)O^{18}$ reaction. This is because ^{18}F which is unstable against β-decay and at low density such as $\rho_2(=\rho/10^2$ g/cm^3)$=1$ and, for temperature $0.02 \leq T_9 \leq 0.1$, the p-capture lifetime of ^{18}F is very large as compared to its β decay mean lifetime ie 9504 sec (Audi et al. (2003)[256]). ^{18}O the tertiary isotope of oxygen has very low abundance compared to ^{16}O but greater as compared to ^{17}O

(Lodders (2003)[257]). This point onwards we take the reaction steps given in (Hansen et al.(2004)[260], Mountford (2013)[261]) ie ^{18}O(p,γ)^{19}F. Sometime the radiative capture on ^{18}O can't be neglected as compared to O^{18}(p,α)N^{15} even though the (p,α) channel is substantially stronger then (p,γ) channels. Because depending upon the spin and energy of resonance the latter can be of comparable strength (Weischer et al. (1980)[262]). Still we have checked for possible alteration of abundances of oxygen by including of a third branching point at ^{18}O. But still it doesn't lead us to find any significant change in the mass fraction of ^{16}O which has been found to be consistent with the earlier report of Audouze (1976)[263] where the author had mentioned that the ^{18}O(p,γ)^{19}F leak has little effect on CNO equilibrium abundance. For instance the ^{16}O abundance changes by 12% only, at temperatures T_9=0.03 and 0.05 (Table 4.5). Moreover the goal of this choice is because it may improve our knowledge of levels in the ^{19}F nucleus that are relevant to nuclear astrophysics and hopefully for a possible fluorine production network. Recently Buckner et al. (2012)[264] had studied ^{18}O(p,γ)^{19}F reaction and have found that most ^{19}F levels decay by $\gamma\gamma$-cascades through the first (110 keV) excited state, and all ^{19}F levels (with known decay schemes) de-excite through the second (197 keV) excited state. Moreover it is an interesting element in the periodic table because of the fact that though it is surrounded by some of the most abundant elements in the universe like oxygen, nitrogen and neon, yet it is itself very rare. Perhaps it is because an odd Z element with only one single stable isotope and it is very fragile with its 9 protons and 10 neutrons (Palacois (2006)[265]). Then the finally produced ^{19}F which is destroyed by a (p,α) reaction forming ^{16}O since ^{19}F(p,α)^{16}O (p,α) reaction rate is faster as compared to (p,γ) reaction which would have produced ^{20}Ne. Thus the CNOF cycle is

$$
\begin{aligned}
^{12}C + p &\longrightarrow ^{13}N + \gamma \\
^{13}N &\longrightarrow ^{13}C + e^{+} + \nu_e \\
^{13}C + p &\longrightarrow ^{14}N + \gamma \\
^{14}N + p &\longrightarrow ^{15}O + \gamma \\
^{15}O &\longrightarrow ^{15}N + e^{+} + \nu_e \\
^{15}N + p &\longrightarrow ^{12}C + \alpha \\
^{15}N + p &\longrightarrow ^{16}O + \gamma \\
^{16}O + p &\longrightarrow ^{17}F + \gamma \\
^{17}F &\longrightarrow ^{17}O + e^{+} + \nu_e \\
^{17}O + p &\longrightarrow ^{14}N + \alpha \\
^{17}O + p &\longrightarrow ^{18}F + \gamma \\
^{18}F &\longrightarrow ^{18}O + e^{+} + \nu_e \\
^{18}O + p &\longrightarrow ^{19}F + \gamma \\
^{19}F + p &\longrightarrow ^{16}O + \alpha
\end{aligned}
$$

Table 4.1 The branching ratio ($B_r = \frac{N_A<\sigma v>_{p,\gamma}}{N_A<\sigma v>_{p,\alpha}}$) at various T_9 values.

T_9	$^{15}N(B_r)$	$^{17}O(B_r)$
0.02	4.615×10^{-4}	1.312×10^{-1}
0.03	4.232×10^{-4}	5.601×10^{-3}
0.05	3.652×10^{-4}	4.031×10^{-3}
0.08	3.134×10^{-4}	5.745×10^{-3}
0.1	2.857×10^{-4}	7.722×10^{-3}

NeNa cycle:

At high temperature conditions additional hydrogen burning cycles may come in the form of NeNa cycle (Marion et al. (1957)[266]). Because of the high coulomb barrier they may not be seem important from the energy sources point of view. However, the enhancement of Na which has been observationally found in many red giant and supergiant stars demands the investigation of NeNa cycle as a possible candidate of Na enhancement. Typically this cycle starts from Ne^{20} which capture a proton to form Na^{21}. This unstable Na^{21} forms Ne^{21}

via a β emission. However the reaction $Ne^{21}(\alpha,n)Mg^{24}$ can be a source of neutron (B2FH (1957)[83]) if α particles are available but the branching ratio $(\frac{N_A<\sigma v>_{\alpha,n}}{N_A<\sigma v>_{p,\gamma}})<<1$ guarantees the production of Na^{22} through $Ne^{21}(p,\gamma)Na^{22}$ which is a relatively long-lived isotope of Na with an average lifetime of 1.183×10^8 sec. Na^{22} produces Ne^{22} via $Na^{22}(e^+,\nu_e)Ne^{22}$. We have also taken into account of the reaction $Na^{22}(p,\gamma)Mg^{23}$ that may affect the energy production rate, cycle lifetime and the abundance of Na. Other β-decay life times can not compete with the proton-capture lifetime so long as the value of temperature $T_9 \leq 0.05$. Production of Mg^{25} from Ne^{22} via (α,n) reaction is ignored as the temperature required $(T_9 = 0.3)$ for this reaction to occur is beyond the temperature range we have considered. The reactions in the NeNa cycle will depend upon the competition between proton capture and β-decay lifetimes which again in turn depend upon the density and temperature condition. These factors are taken into account, and thus the NeNa cycle as below:

$$
\begin{aligned}
^{20}Ne + p &\longrightarrow^{21} Na + \gamma \\
^{21}Na &\longrightarrow^{21} Ne + e^+ + \nu_e \\
^{21}Ne + p &\longrightarrow^{22} Na + \gamma \\
^{22}Na &\longrightarrow^{22} Ne + e^+ + \nu_e \\
^{22}Ne + p &\longrightarrow^{23} Na + \gamma \\
^{23}Na + p &\longrightarrow^{20} Ne + \alpha
\end{aligned}
$$

Thus Ne^{20} can be formed when Na^{23} captures a proton as the nuclear reaction rates for $Na^{23}(p,\alpha)Ne^{20}$ is higher $(10-10^2)$ (Iliadis et al. (2010)[133]) compared to the competing reaction $Na^{23}(p,\gamma)Mg^{24}$ which is sufficient to guarantee NeNa cycling.

MgAl cycle:

This cycle, initiated by Mg^{24} with a proton-capture leads to the formation of unstable Al^{25}. Mg^{24} is the most abundant element of the cycle for temperature $T_9 \leq 0.05$ because of the slow reaction rate of $Mg^{24}(p,\gamma)Al^{25}$. Al^{25} quickly disintegrates to Mg^{25} in an average time

scale of 10.365 sec (Audi et al. (2003)[256]). Mg^{25} through a (p,γ) reaction forms the other isotopes of Al. The first one is Al^{26} which exists in two states, a ground state Al^{26g} and an isomeric state Al^{26m}. If temperature $T_9 \geq 1$, both Al^{26g} ($T_\beta = 3.262 \times 10^{13}$ sec; (Audi et al. (2003)[256]) and Al^{26m} ($T_\beta = 9.155$ sec; (Audi et al. (2003)[256]) quickly attains equilibrium. At $T_9 \leq 0.4$ (which falls within the temperature range considered here) the equilibrium does not get established and hence both the species have to be treated separately (Ward et al. (1980)[267]). Thus, if the temperature $T_9 < 0.03$, destruction of Al^{26g} mainly occurs through a β-decay reaction at both the density values considered here. Assuming this isotope of Al to be stable we have considered Al^{26g}(p,γ)Si^{27}(e^+,ν_e)Al^{27} at the considered range of temperatures. The destruction of Al^{27} again depends upon the stellar temperature. As long as the temperature T_9 remains less than 0.08 the (p,α) reaction wins over (p,γ) reaction (Iliadis et al. (2010)[133]) and that is sufficient to confirm the cyclic nature of Mg-Al burning modes. But if T_9 goes beyond that value there will be leakage of Al^{27} through Al^{27}(p,γ)Si^{28} which is being ignored in the present case. For the MgAl cycle the following reaction chains are being considered.

$$
\begin{aligned}
^{24}Mg + p &\longrightarrow ^{25} Al + \gamma \\
^{25}Al &\longrightarrow ^{25} Mg + e^+ + \nu_e \\
^{25}Mg + p &\longrightarrow ^{26g} Al + \gamma \\
^{26g}Al + p &\longrightarrow ^{27} Si + \gamma \\
^{27}Si &\longrightarrow ^{27} Al + e^+ + \nu_e \\
^{27}Al + p &\longrightarrow ^{24} Mg + \alpha
\end{aligned}
$$

4.4 Nuclear Reaction Rate and Lifetime

The rate for a given reaction depends on the number density of the reactants, N_a and N_X , the rate these reactants encounter each other (i.e., their velocity) and on the cross section (σ) for

the reaction which is given by

$$\sigma = \frac{\text{number of reactions/nucleus X/unit time}}{\text{number of incident particles/cm}^2\text{/unit time}}$$

The cross section itself is going to be a function of particle velocity (v) as there are electrostatic repulsion between the reactants. Thus the reaction rate can be written as

$$R_{aX} = N_a N_X \, \sigma(v) \, v$$

As the particles in a star have a distribution of velocities, the integration over a velocity distribution, $\phi(v)$ will give the true reaction rate. Moreover if identical particle are involving then the actual reaction rate will be

$$\begin{aligned} R_{aX} =& \frac{1}{1+\delta_{aX}} N_a N_X \int_0^\infty \sigma(v) \, v \, \phi(v) \, dv \\ =& \frac{1}{1+\delta_{aX}} \left(\frac{\rho^2 N_A X_a X_X}{A_a A_X} \right) [N_A < \sigma v >] \quad cm^{-3} sec^{-1} \end{aligned}$$

For computational simplification the number density N_a of any element with mass number A_a has been expressed in terms of its mass fraction X_a by $N_a = \rho X_a N_A / A_a$. Here ρ is the density, N_A is Avogadro's number and $N_A < \sigma v >$ is the reaction rate constant. Similar treatment is also done for N_X too. From this the lifetime against proton-capture for the elements in the enhanced state is given by the following equation

$$\tau_p = \frac{1}{\rho X_H [N_A < \sigma v >]} \quad sec \tag{4.1}$$

4.4.1 Lifetimes of CNOF reactions

To calculate the lifetimes of all the reactions at the density value, the required reaction rate constants are taken from Iliadis et al. (2010)[133] which are the recommended medium

rate constant values except for the (p,α) reactions. The reaction rate constants for the (p,α) reactions reaction, involved in this cycle have been taken from NACRE compilation. Estimated proton-capture lifetimes for various elements are listed in Table 4.2 which are relevent to our reaction cycle.

Table 4.2 $N_A < \sigma v >$ are in $cm^3 mol^{-1} sec^{-1}$, T_9 is in the unit of 10^9 K and ρ_2 is in the unit of 10^2 gm cc^{-1}. τ_β for ^{13}N,^{15}O,^{17}F and ^{18}F are 862.77, 176.39, 93.059 and 9504 sec respectively. τ_p is the proton-capture lifetimes in sec.

Reaction	T_9	$N_A < \sigma v >$	$\tau_p(\rho_2 = 1)$
	0.02	3.76×10^{-14}	3.79×10^{11}
	0.03	1.74×10^{-11}	8.21×10^{8}
$^{12}C(p,\gamma)^{13}N$	0.05	1.31×10^{-8}	1.09×10^{6}
	0.08	2.28×10^{-6}	6.26×10^{3}
	0.1	2.03×10^{-5}	7.03×10^{2}
	0.02	1.89×10^{-13}	7.55×10^{10}
	0.03	8.77×10^{-11}	1.62×10^{8}
$^{13}C(p,\gamma)^{14}N$	0.05	6.49×10^{-8}	2.20×10^{5}
	0.08	1.10×10^{-5}	1.29×10^{3}
	0.1	9.60×10^{-5}	1.48×10^{2}
	0.02	4.11×10^{-16}	3.47×10^{13}
	0.03	3.85×10^{-13}	3.71×10^{10}
$^{13}N(p,\gamma)^{14}O$	0.05	6.15×10^{-9}	2.32×10^{5}
	0.08	1.93×10^{-7}	7.40×10^{4}
	0.1	2.19×10^{-5}	6.52×10^{2}
	0.02	1.59×10^{-16}	8.98×10^{13}
	0.03	1.45×10^{-13}	9.85×10^{10}
$^{14}N(p,\gamma)^{15}O$	0.05	2.21×10^{-10}	6.46×10^{7}
	0.08	6.50×10^{-8}	2.19×10^{5}
	0.1	7.20×10^{-7}	1.98×10^{4}
	0.02	3.90×10^{-15}	3.66×10^{12}
	0.03	3.70×10^{-12}	3.86×10^{9}
$^{15}N(p,\gamma)^{16}O$	0.05	5.97×10^{-9}	2.39×10^{6}
	0.08	1.89×10^{-6}	7.55×10^{3}
	0.1	2.16×10^{-5}	6.61×10^{2}
	0.02	5.45×10^{-47}	2.62×10^{44}
	0.03	1.25×10^{-43}	1.14×10^{41}
$^{15}O(p,\gamma)^{16}F$	0.05	6.66×10^{-37}	2.14×10^{34}
	0.08	1.34×10^{-34}	1.06×10^{32}
	0.1	4.64×10^{-33}	3.07×10^{30}

Reaction	T_9	$N_A < \sigma v >$	$\tau_p(\rho_2 = 1)$
$^{16}O(p,\gamma)^{17}F$	0.02	3.78×10^{-18}	3.77×10^{15}
	0.03	6.59×10^{-15}	2.16×10^{12}
	0.05	1.98×10^{-11}	7.21×10^{8}
	0.08	9.71×10^{-9}	1.47×10^{6}
	0.1	1.30×10^{-7}	1.09×10^{6}
$^{17}F(p,\gamma)^{18}Ne$	0.02	6.12×10^{-21}	2.33×10^{18}
	0.03	2.15×10^{-17}	6.64×10^{14}
	0.05	1.36×10^{-13}	1.05×10^{11}
	0.08	1.24×10^{-10}	1.15×10^{8}
	0.1	2.17×10^{-9}	6.58×10^{6}
$^{17}O(p,\gamma)^{18}F$	0.02	2.08×10^{-18}	6.86×10^{15}
	0.03	9.69×10^{-15}	1.47×10^{12}
	0.05	7.62×10^{-11}	1.87×10^{8}
	0.08	1.58×10^{-8}	9.04×10^{5}
	0.1	1.39×10^{-7}	1.02×10^{5}
$^{18}F(p,\gamma)^{19}Ne$	0.02	5.47×10^{-17}	2.61×10^{14}
	0.03	6.84×10^{-14}	2.08×10^{11}
	0.05	2.57×10^{-11}	5.55×10^{8}
	0.08	3.88×10^{-9}	3.68×10^{6}
	0.1	3.93×10^{-8}	3.63×10^{3}
$^{18}O(p,\gamma)^{19}F$	0.02	1.2×10^{-17}	1.19×10^{15}
	0.03	1.79×10^{-14}	7.98×10^{11}
	0.05	1.35×10^{-10}	1.05×10^{8}
	0.08	7.11×10^{-6}	2.00×10^{3}
	0.1	3.17×10^{-4}	4.50×10^{1}
$^{19}F(p,\alpha)^{16}O$	0.02	3.76×10^{-17}	3.79×10^{14}
	0.03	1.33×10^{-13}	2.07×10^{9}
	0.05	8.72×10^{-10}	1.63×10^{7}
	0.08	9.71×10^{-9}	1.47×10^{6}
	0.1	1.65×10^{-5}	8.65×10^{2}

4.4.2 Lifetimes of NeNa reactions

In Table 4.3 we present the proton-capture lifetimes for various elements at considered stellar condition. The reaction rate constants are taken from Iliadis et al. (2010)[133].

Table 4.3 $N_A < \sigma v >$ are in $cm^3 mol^{-1} sec^{-1}$, T_9 is in the unit of 10^9 K and ρ_2 is in the unit of 10^2 gm cc^{-1}. τ_β for ^{21}Na and ^{22}Na are 32.453 and1.18×10^8 sec respectively. τ_p is the proton-capture lifetimes in sec.

Reaction	T_9	$N_A < \sigma v >$	$\tau_p(\rho_2 = 1)$
$^{20}Ne(p,\gamma)^{21}Na$	0.02	3.07×10^{-21}	4.65×10^{20}
	0.03	1.39×10^{-19}	1.03×10^{17}
	0.05	1.15×10^{-13}	1.24×10^{11}
	0.08	1.23×10^{-10}	1.16×10^{8}
	0.1	2.29×10^{-9}	6.24×10^{6}
$^{21}Na(p,\gamma)^{22}Mg$	0.02	1.15×10^{-24}	1.24×10^{22}
	0.03	1.38×10^{-20}	1.04×10^{18}
	0.05	3.62×10^{-16}	3.95×10^{13}
	0.08	7.77×10^{-10}	1.84×10^{7}
	0.1	2.17×10^{-7}	6.58×10^{4}
$^{21}Ne(p,\gamma)^{22}Na$	0.02	5.36×10^{-22}	2.67×10^{19}
	0.03	9.42×10^{-18}	1.52×10^{15}
	0.05	3.53×10^{-10}	4.05×10^{7}
	0.08	6.45×10^{-6}	2.22×10^{3}
	0.1	1.54×10^{-4}	9.28×10^{1}
$^{22}Na(p,\gamma)^{23}Mg$	0.02	5.19×10^{-20}	2.75×10^{17}
	0.03	2.2×10^{-16}	6.49×10^{13}
	0.05	1.37×10^{-12}	1.04×10^{10}
	0.08	3.41×10^{-9}	4.19×10^{6}
	0.1	6.93×10^{-7}	2.06×10^{4}
$^{22}Ne(p,\gamma)^{23}Na$	0.02	1.96×10^{-16}	7.29×10^{13}
	0.03	1.01×10^{-13}	1.41×10^{11}
	0.05	1.15×10^{-11}	1.24×10^{9}
	0.08	3.84×10^{-10}	3.72×10^{7}
	0.1	9.18×10^{-9}	1.56×10^{6}
$^{23}Na(p,\alpha)^{20}Ne$	0.02	5.58×10^{-22}	2.56×10^{19}
	0.03	6.55×10^{-18}	2.18×10^{15}
	0.05	2.28×10^{-13}	6.27×10^{10}
	0.08	4.37×10^{-9}	3.27×10^{6}
	0.1	3.35×10^{-7}	4.26×10^{5}

4.4.3 Lifetimes of MgAl reactions

The calculated proton-capture lifetimes have been presented in Table 4.4 for the cycle using the recommended reaction rate constants from Iliadis et al. (2010)[133]. Once again

the nuclear reaction sequence in the MgAl cycle depends on the competition between the proton-capture and β-decay lifetimes.

Table 4.4 $N_A < \sigma v >$ are in $cm^3 mol^{-1} sec^{-1}$, T_9 is in the unit of 10^9 K and ρ_2 is in the unit of 10^2 gm cc^{-1}. τ_β for ^{25}Al,^{26g}Al and ^{27}Si are 10.365, 3.26×10^{13} and 6.002 sec respectively. The τ_p is the proton-capture lifetimes in sec.

Reaction	T_9	$N_A < \sigma v >$	$\tau_p(\rho_2 = 1)$
$^{24}Mg(p,\gamma)^{25}Al$	0.02	4.0×10^{-26}	3.57×10^{23}
	0.03	8.92×10^{-22}	1.60×10^{19}
	0.05	9.94×10^{-17}	1.44×10^{14}
	0.08	3.08×10^{-9}	4.64×10^{6}
	0.1	1.09×10^{-6}	1.31×10^{4}
$^{25}Al(p,\gamma)^{26}Si$	0.02	4.28×10^{-28}	3.34×10^{25}
	0.03	1.63×10^{-23}	8.76×10^{20}
	0.05	2.42×10^{-18}	5.90×10^{15}
	0.08	6.69×10^{-13}	2.14×10^{10}
	0.1	5.39×10^{-11}	2.65×10^{8}
$^{25}Mg(p,\gamma)^{26g}Al$	0.02	3.81×10^{-20}	3.75×10^{19}
	0.03	1.41×10^{-15}	1.01×10^{13}
	0.05	5.57×10^{-12}	2.57×10^{9}
	0.08	1.45×10^{-9}	9.85×10^{6}
	0.1	1.34×10^{-8}	1.07×10^{6}
$^{26g}Al(p,\gamma)^{27}Si$	0.02	4.78×10^{-26}	2.99×10^{23}
	0.03	1.49×10^{-19}	9.57×10^{16}
	0.05	1.25×10^{-13}	1.14×10^{11}
	0.08	7.8×10^{-10}	1.83×10^{7}
	0.1	8.17×10^{-8}	1.75×10^{5}
$^{26}Mg(p,\gamma)^{27}Al$	0.02	6.13×10^{-22}	2.33×10^{19}
	0.03	1.09×10^{-17}	1.31×10^{15}
	0.05	1.02×10^{-12}	1.40×10^{10}
	0.08	3.03×10^{-9}	4.71×10^{6}
	0.1	5.66×10^{-8}	2.52×10^{5}
$^{27}Si(p,\gamma)^{28}P$	0.02	1.78×10^{-23}	8.03×10^{20}
	0.03	6.35×10^{-20}	2.25×10^{17}
	0.05	3.26×10^{-15}	4.38×10^{12}
	0.08	7.13×10^{-11}	2.00×10^{8}
	0.1	3.82×10^{-9}	3.74×10^{6}
$^{27}Al(p,\alpha)^{24}Mg$	0.02	3.07×10^{-25}	4.65×10^{22}
	0.03	1.86×10^{-19}	7.68×10^{16}
	0.05	9.11×10^{-15}	1.57×10^{12}
	0.08	3.84×10^{-12}	3.72×10^{9}
	0.1	4.34×10^{-11}	3.29×10^{8}

4.5 Evolution of Elemental abundances

In the reaction cycle considered, the cycle produces one α-particle along with two ν_es and two e^+s. The initial nuclei act mainly as catalysts. Although there is always a consumption of hydrogen the total mass and the total number of nuclei in each cycle remain conserved. Thus the net effect for all the three cycles is

$$4H^1 \rightarrow He^4 + 2e^+ + 2\nu_e + \gamma, \quad \frac{dN_H}{dt} < 0, \quad \frac{dN_{He}}{dt} > 0 \tag{4.2}$$

The generalised differential equation that governs the evolution of any element in terms of number density via a proton-capture reaction or a β-decay or both at the enhanced condition is given by Clayton (1983)[255]

$$\frac{dN_i}{dt} = -N_i N_H < \sigma v >_{p,i} + N_j N_H < \sigma v >_{H,j} \pm \lambda_k N_k \tag{4.3}$$

where λ_k is the decay constant of an unstable nucleus with number density N_k. As all the three cycles involved proton-capture reactions and β-decays, the abundances will primarily depend upon the lifetime of these processes. If the β-decay lifetimes, τ_β for an unstable element in the cycle is shorter than the proton-capture lifetime τ_p for the same element then the β-decay lifetimes can be bypassed and thus the element can be thought of representing the next stable element in the cycle having the same mass number. Considering that the Eq. 5.3 for each cycle takes the form of the following differential rate equations in terms of mass fraction of any element

$$\frac{dX_i}{dt} = \left(-R_{p,i} X_i X \rho + \frac{A_i}{A_j} R_{p,j} X_j X \rho \right) \tag{4.4}$$

where $R_{p,i}$s are $[N_A < \sigma v >]$ terms for the respective proton-capture reactions. A_i and A_j stand for mass number of different nuclei. Eq. 5.4 can be expressed as a function of the

hydrogen mass fraction to get a series of first order simultaneous linear differential equations for each cycle as

$$\frac{dX_i}{dX_H} = \frac{\left(-R_{p,i}X_i + \frac{A_i}{A_j}R_{p,j}X_j\right)}{\left[-\sum_{A_i}^{A_j}\left(\frac{1}{A_i}R_{p,i}X_i\right)\right]} \tag{4.5}$$

which are then solved for suitable initial condition. The equilibrium abundance by mass fraction of the stable isotopes of considered elements are taken up to the first decimal place. The N^{14} abundance is found to highest amongst all while the abundance of O^{16} is higher compared to the abundances of other isotopes of oxygen, but does not show any significant variation. This is probably because these two isotopes are circulated back by $O^{17}(p,\alpha)N^{14}$ and $F^{19}(p,\alpha)O^{16}$ respectively. In NeNa cycle, Na does show a variation with respect to increase in temperature. This is probably directly reflected on increase in Ne^{20} abundance and in MgAl cycle the elements present here show their signature only at temperature greater than $T_9 = 0.03$ and they do show noticeable variation with respect to temperature again, abundance of Mg^{24} decreases with respect to temperature at a steeper slope. Thus at higher temperature more of Mg^{25} will be present which in turn will influence he production of Al^{26g} which also decreases slowly with increase in temperature. These decrements have resulted in increase of the Al^{27} isotope. The abundance by mass fraction has shown in the Fig. 4.3.

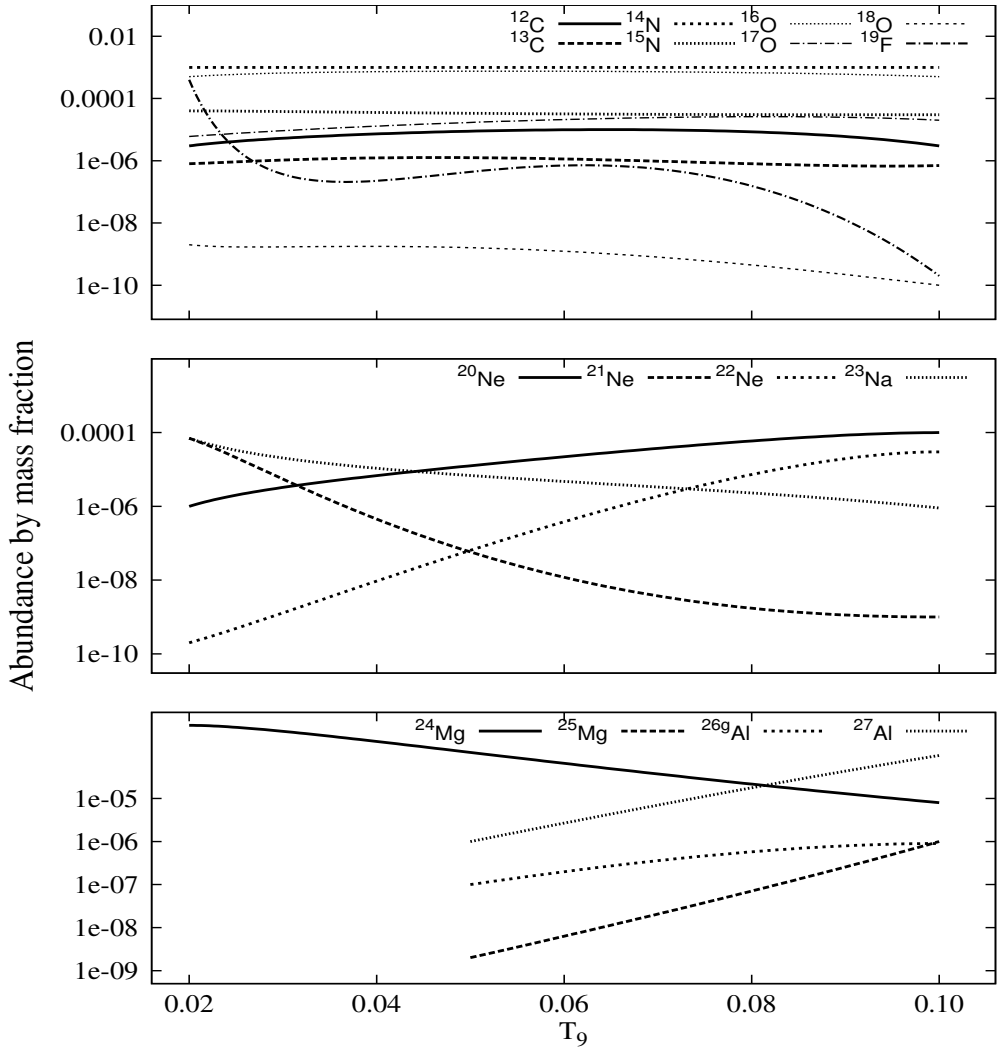

Fig. 4.3 Profiles of equilibrium abundances by mass fraction of stable isotopes with respect to temperature are shown for the stable nuclides in the CNOF cycle (top panels), NeNa cycle (middle panels) and MgAl cycle (bottom panels) at density $\rho_2 = 1$ gm cc^{-1}.

4.5.1 Calculation of abundances

In the case of CNOF cycle the initial abundance of heavy elements have been chosen in such a manner that it does not affect the production of primary nitrogen from being the highest abundant element in the CNO reaction, which actually gets hampered for metallicities higher than Z= 0.001. Moreover at higher metallicities the rotational mixing is not so efficient. Neither we take very or extremely low metallicities because low metallicity reveals a low content of heavy elements and thereby making the opacity lower. Hence the stars become more compact, and therefore hotter so they are going to have high luminosity. This high luminosity increases the radiation pressure and thus stellar mass loss (Meynet et al. (2009)[271]). Again in the case of fast rotating massive stars, with an initial metallicity Z= 0.0005, with typical time averaged velocity of 500 kms^{-1} on the main sequence easily reach the critical velocity (Decressin et al. (2007b)[130]) at the beginning of their evolution and remain near the critical limit during the rest part of their main sequence. As a consequence, they lose large amount of material through a mechanical wind, which probably leads to the formation of a slow outflowing Keplerian equatorial disk. Keeping in view of all these the simultaneous linear first order differential equations are solved numerically for each cycle varying the hydrogen mass fraction up to $X = 0.60$ to get the equilibrium mass fraction abundances of the stable heavy elements with the initial condition as $X = 0.70$, $Y = 0.298$, such that $X + Y + Z = 1$ where Z is the sum of the mass fraction of elements C^{12},N^{14},O^{16},and F^{19} distributed equally ie $Z_{C^{12}} = Z_{N^{14}} = Z_{O^{16}} = Z_{F^{19}} = 0.0005$ for CNOF then $X = 0.70$, $Y = 0.2995$, $Z_{Ne^{20}} = 0.0005$ for NeNa and lastly $X = 0.70$, $Y = 0.2995$, $Z_{Mg^{24}} = 0.0005$ for MgAl cycle (Meynet et al. (2008)[272]). Abundance by mass fraction thus obtained for any stable element (x) with respect to Fe are then calculated using the expression

$$\left[\frac{x}{Fe}\right] = \left[\frac{x}{H}\right] - \left[\frac{Fe}{H}\right] \tag{4.6}$$

Here

$$\left[\frac{x}{H}\right] = log\left[\frac{N_x}{N_H}\right]_{star} - log\left[\frac{N_x}{N_H}\right]_{\odot}$$

and

$$\left[\frac{Fe}{H}\right] = log\left[\frac{N_{Fe}}{N_H}\right]_{star} - log\left[\frac{N_{Fe}}{N_H}\right]_{\odot}$$

The quantities $N_x\odot$ and $N_H\odot$ are the solar number densities taken from (Lodders (2003)[257]). For oxygen we have taken the equilibrium O^{16} mass fraction for the abundance calculations since its relative abundance is larger compared to the other two stable isotopes of oxygen.

4.5.2 Uncertainty in calculation

We have also calculated the range of uncertainty in the equilibrium mass fraction abundance of O^{16}, Na^{23} and Al^{27}, due to the uncertainty in the reaction rate constants, considering both low and high rate constants for respective reactions taken from (Iliadis et al. (2010)[133]) as well as NACRE compilation. These are presented in Table 4.5. The calculated abundances

Table 4.5 The derived abundance of O^{16}, Na^{23} and Al^{27} due to low, medium and high reaction rate constant values.

T_9	O^{16}			Na^{23}			Al^{27}		
	Low	Medium	High	Low	Medium	High	Low	Medium	High
0.02	5×10^{-4}	5×10^{-4}	5×10^{-4}	6×10^{-5}	7×10^{-5}	1×10^{-4}	****	*****	*****
0.03	6×10^{-4}	8×10^{-4}	6×10^{-4}	1×10^{-5}	1×10^{-5}	5×10^{-6}	****	*****	*****
0.05	7×10^{-4}	8×10^{-4}	8×10^{-4}	1×10^{-5}	6×10^{-6}	6×10^{-6}	3×10^{-6}	1×10^{-6}	8×10^{-7}
0.08	7×10^{-4}	8×10^{-4}	8×10^{-4}	3×10^{-6}	3×10^{-6}	4×10^{-6}	2×10^{-5}	2×10^{-5}	2×10^{-5}
0.10	8×10^{-4}	5×10^{-4}	8×10^{-4}	1×10^{-6}	9×10^{-7}	1×10^{-6}	4×10^{-5}	1×10^{-5}	2×10^{-5}

of O, Na and Al are presented in Appendix C.1, C.2, C.3 and C.4,for density $\rho_2 = 1$ for the clusters M3, M4, M13 and NGC6752 respectively. The observed abundances of a few metal poor evolved stars from (Cohen et al. (2005)[225], Ivans et al. (1999)[75], Cohen et al. (2005)[225] and Yong et al. (2005)[33]) are also presented in these tables for a comparison. The calculated abundances at a particular temperature are those for which the difference between the observed and the calculated abundance is found to be minimum. Here most

of the stars have gotten impacted since the influence of the wind is necessary in order to explain the GC abundance anomalies (Decressin et al. (2007b)[130]). Moreover, the second generation of stars are formed because of the ejection of material from the rapidly rotating massive stars which are mixed with primordial material left over from the star formation process (Bastian et al. (2014)[273]). A recent study conducted by Bekki (2011)[258] has shown that in massive star clusters second generation of stars are formed from the gaseous ejecta of AGB stars if the mass of cluster exceeds $10^6 M_{\odot}$. Thus this gives a possibility of the presence of many massive stars within the same GC. A comparison between the computed and observed abundances from Cohen et al. (2005)[225], Ivans et al. (1999)[75] and Yong et al. (2005)[33]) is shown in Fig. 4.8 (top right, top left, bottom right and bottom left respectively for the stars belonging to the four GCs. In Fig. 4.9 we have shown the anticorrelation trends between the O and Na amongst the stars of our GCs with the computed ratios of [Na/Fe] and [O/Fe] from this work are compared with their counterparts observed in the evolved stars of the all four globular clusters M3 (top left (Cohen et al. (2005)[225])), M4 (top right (Ivans et al. (1999)[75])), M13 (bottom left (Cohen et al. (2005)[225])) and NGC6752 (bottom right (Yong et al. (2005)[33])).

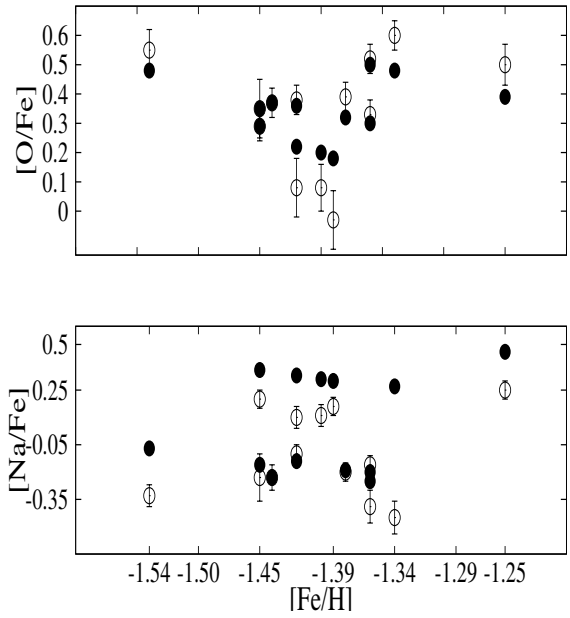

Fig. 4.4 M3

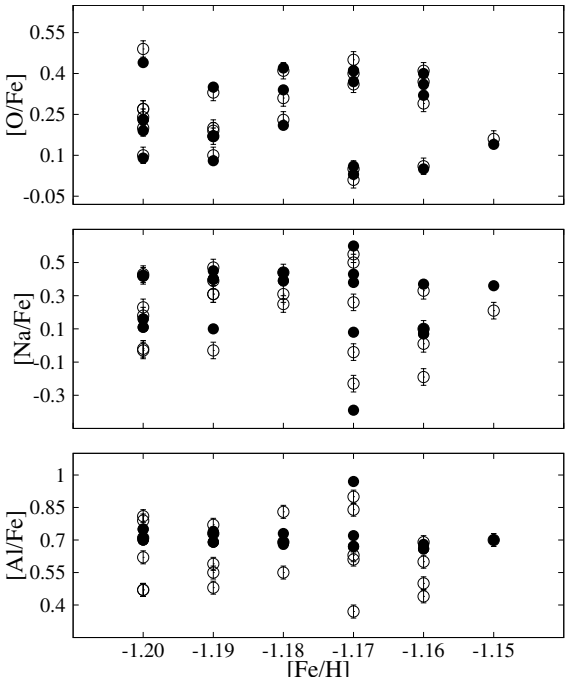

Fig. 4.5 M4

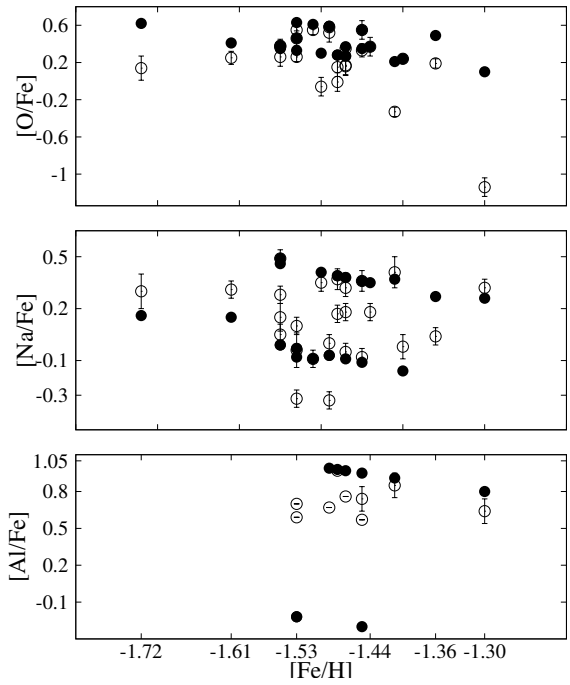

Fig. 4.6 M13

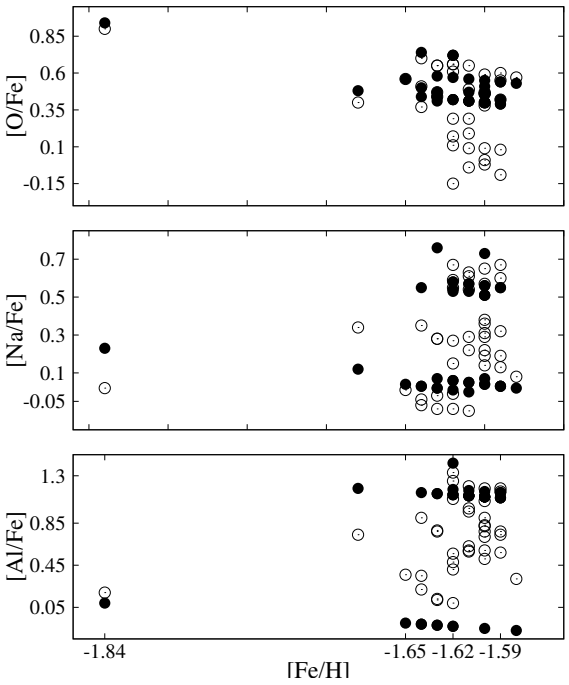

Fig. 4.7 NGC 6752

Fig. 4.8 A comparative view od abundance ratios of [O/Fe], [Na/Fe] and [Al/Fe]. Here solid circles:"this work" and open circles: (Yong et al. (2005)[33] for GC M3 and NGC 6752; Ivans et al. (1999)[75] for M4 and Cohen et al. (2005)[225] for M13.

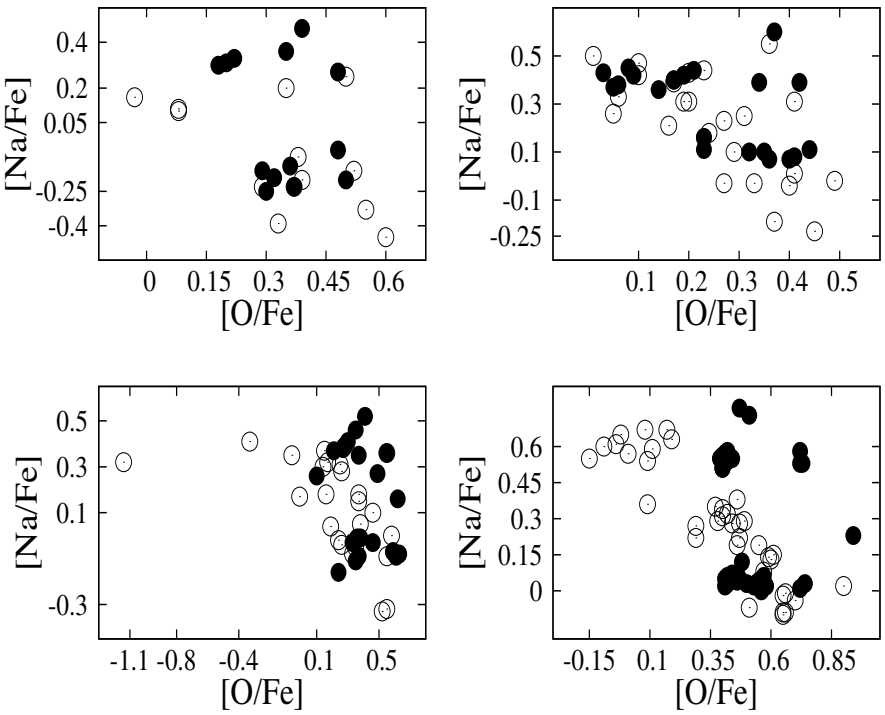

Fig. 4.9 Observed Na-O relation. Here solid circles corresponds to the data points of "this work" and open circles are from literature

4.6 Summary

Elemental abundance patterns of Globular Cluster stars can provide important clues for understanding cluster formation and early chemical evolution. The origin of the abundance patterns, however, still remains poorly understood. We have studied the impact of p-capture reaction cycles on the abundances of oxygen, sodium and aluminium considering nuclear reaction cycles namely CNOF, NeNa and MgAl in massive stars in stellar conditions of temperature range, 2×10^7 to 10×10^7 K and typical density of 10^2 gm/cc. We have estimated abundances of oxygen, sodium and aluminium with respect to Fe, which are then assumed to be ejected from those stars because of rotation, rotating at the critical limit. These ejected abundance of elements are then compared with their counterparts what has been observed

in some metal-poor evolved stars, mainly giants and red-giants, of globular clusters M3, M4, M13 and NGC6752. We observe an excellent agreement with [O/Fe] between the estimated and observed abundance values for globular clusters M3 and M4 with a correlation coefficient above 0.9 and a strong linear correlation for the rest of two clusters with a correlation coefficient above 0.7. Then the estimated [Na/Fe] and [Al/Fe] ratios are found to have a correlation coefficient above 0.7, thus implying a strong correlation for all the four globular clusters except in GC M4 where Al abundance bears a moderate correlation with coefficient above 0.6. Possible sources of these discrepancies have also been discussed.